 CMES, vol.118, no.2, pp.275-290, 2019

Residual Stresses in Resistance Spot Welded AZ61 Mg Alloy

Davood Afshari[1, *], Soheil Mirzaahamdi[1] and Zuheir Barsoum[2]

Abstract: The use of magnesium alloys has been rapidly increased due to their ability to maintain high strengths at light weights. However weldability of steels and aluminum alloys by using resistance spot weld (RSW) process is a major issue, because it cannot be directly utilized for magnesium alloys. In this study, a structural-thermal-electrical finite element (FE) model has been developed to predict the distribution of residual stresses in RSW AZ61 magnesium alloy. Thermophysical and thermomechanical properties of AZ61 magnesium alloy have been experimentally determined, and have been used in FE model to increase the accuracy of the model. X-ray diffraction (XRD) technique has been utilized to measure the residual stresses in welded samples, and its results have been used to validate the FE model. Comparison study shows that the results obtained by using FE model have a good agreement with the experimental XRD data. In specific, the results show that the maximum tensile residual stress occurs at the weld center while decreases towards the nugget edge. In addition, the effects of welding parameters such as electrical current, welding time, and electrode force have been investigated on the maximum tensile residual stress. The results show that the tensile residual stress in welded joints rises by increasing the electrical current; however, it declines by prolonging the welding time as well as increasing the electrode force.

Keywords: Resistance spot weld, AZ61 mg alloy, residual stresses, finite element model, x-ray diffraction.

1 Introduction

Magnesium and its alloys are considered as green engineering materials and one of the most promising special metal groups of the twenty-first century. Being a light weight material, magnesium has a low density approximately one fourth that of steel and two thirds of aluminum. It has high specific strength higher than that of aluminum and iron in the ratio of 14.1% and 67.7%, respectively [Manladan, Yusof, Ramesh et al. (2016)]. However, weldability of steels and aluminum alloys by RSW process is recognized, it cannot be directly utilized for magnesium alloys, because of higher thermal conductivity and high coefficient of thermal expansion. Moreover, low melting temperature, wide solidification temperature range, and high solidification range influence weldability of magnesium alloys [Kramar, Vondrous, and Kolarikava (2015)].

[1] University of Zanjan, Zanjan, 45371-38791, Iran.

[2] Department of Aeronautical and Vehicle Engineering, Royal Institute of Technology, Stockholm, SE-100 44, Sweden.

[*] Corresponding Author: Davood Afshari. Email: dasfahri@znu.ac.ir.

In RSW, two overlapping metal plates are located between two water-cooled electrodes; pressure is then exerted on the upper electrode to keep the work pieces together, to produce a first contact between plates. Then, an electrical current is prepared by electrodes in a short time. According to resistance of plates to the flow of a localized and concentrated electrical current, the heat is generated and a molten nugget is formed at the faying surface of plates. The electrical current is turned off after the welding step and the nugget would start to solidify and get cool to room temperature. Also, phase change occurs in solidifying metal, causing residual stresses to remain in RSW joint.

It is accounted that the residual stresses may cause brittle fracture, crack propagation, fatigue life decrease, and stress corrosion cracking [Parmar (1999); Ranjbar Nodeh, Serajzadeh and Kokabi (2008); Afshari, Sedighi, Karimi et al. (2013)]. Cha et al. [Cha and Na (2003)] studied the influence of the RSW conditions on the distribution of residual stresses in the 304 stainless steel plates with 2 mm thickness. Zaeem et al. [Zaeem, Nami and Kadivan (2007)] accomplished FE analysis on the residual stress prediction for thin wall aluminum weld structures. In another work accomplished by James et al. [James, Webster, Hughes et al. (2006)] the relationship between the weld process conditions and the residual stresses in high strength steel plates were studied. A 3-D FE welding simulation was carried out on a multi-pass MAG-welded tubular joint structure by Barsoum [Barsoum (2013)]. The calculated temperatures and residual stresses were compared with the experimental data. There was a good agreement between the results obtained from the FE model and the residual stresses measured experimentally. A 2-D mathematical model was created to analyze the distribution of the residual stresses after RSW of steel, as well as to study the influences of welding parameters on residual stress distribution, and conclusions of simulation were compared with the experimental data reaching from X-ray diffraction by Ranjbar Nodeh et al. [Ranjbar Nodeh, Serajzadeh and Kokabi (2008)].

Florea et al. [Florea, Hubbard, Solanki et al. (2012)] examined the 3-D residual stress fields distinguished as in-plane longitudinal, transversal stress, and normal stress for a RS welded joint of 6061-T6 aluminum alloy. Satonaka et al. [Satonaka, Lwamoto, Matsumoto et al. (2012)] investigated the RSW of magnesium alloy sheets with cover plates. The effects of the welding conditions on the nugget size, formation of blowholes, shrinkage cavities, and mechanical strength were studied in this research. Afshari et al. [Afshari, Sedighi, Karimi et al. (2013)] created an axisymmetric model according to an incremental thermo-electro- mechanical coupled FE analysis to predict the residual stresses in RS welded joints of 6061-T6 aluminum alloy. A 2-D FE model was created based on fully coupled electrothermal and incrementally coupled thermomechanical analysis. The influences of welding time and electrical current on distribution and amount of welding residual stresses were also considered by Moshayedi et al. [Moshayedi and Sattari-far (2014)]. Pakkanen et al. [Pakkanen, Vallant and Kiein (2016)] simulated RSW of advanced high strength steel DP1000 with Sysweld^{TM} software. The results obtained from FE model were compared with experimental data obtained from the residual stresses and nugget sizes measurement. Moharrami et al. [Moharrami and Hemmati (2017)] created an appropriate a 3-D FE model by using Ansys software to simulate the process. Fully coupled electrothermal analysis was utilized to obtain residual stress distribution in the welding steps.

The literature review indicates that, however the residual stresses occurred in RSW of steel and aluminum alloys joints have been studied by many researchers, studies on magnesium alloys are rare. In this article, an axisymmetric thermo-electrical-mechanical coupled FE model has been utilized to predict the residual stresses in RSW AZ61 magnesium alloy. Material properties containing physical, thermal, and mechanical properties have been measured experimentally in order to increase the accuracy of the FE model. The whole welding process including squeeze, welding, and holding have been simulated in the FE model. The XRD method has been employed to measure the residual stresses in welding samples to validate the FE model. Finally, the effects of the welding parameters on the tensile radial residual stress have been investigated by the FE model.

2 Experimental procedures

AZ61 magnesium sheet with the dimensions of 100×25×1.2 mm has been used to weld samples. The RSW parameters have been selected based on welding parameters recommended by ASME [ASME (2002)] to achieve acceptable nugget size). RSW has been performed by using a Novin Sazan Company Machine (model SSA014, IRAN) with CU08 controller and copper electrode with nominal welding power of 120 KVA.

The welded samples have been cut along the center of the nugget, and prepared to measure the nugget size. In addition, SEIFERT X-ray diffractometer (model 3000PTS) has been used to measure the residual stresses of 2 welded samples. Measurements have been performed with 1mm diameter probe in 6 different locations (three points are on the left side of nugget and the others are on the right side of nugget) with 5 mm, 7.5 mm, 10 mm distance from the nugget center on the surface of sheet as shown in Fig. 1. For each point the residual stresses have been measured and recorded in radial and transverse directions, and after that the mean residual stress at each two points located on both side of nugget with equal distance has been calculated.

In this study, all the physical, mechanical, and thermal properties of AZ61 have been experimentally measured to increase the accuracy of the FE model. The thermal dependent tensile test has been performed by using a STM 250 machine manufactured by Santam Company. Due to small size of samples, the furnace of the device has not been used but instead, the ceramic element has been used to increase temperature up to 500℃. K-type thermocouple has been utilized to check the temperature of the samples and a two-relay thermostat manufactured by Shiraz instrumentation (model SHD72A, IRAN) has been used to display and check the temperature of the ceramic element and the thermocouple.

Fig. 2 shows the thermal-dependent tensile test. The yield strength of AZ61 magnesium alloy sheet decreases, while the temperature rises up. Therefore, the samples have been failure with low magnitude of tensile forces. All the properties have been measured up to 400°C. Fig. 3 presents the results of the thermal-dependent properties of AZ61 mg alloy.

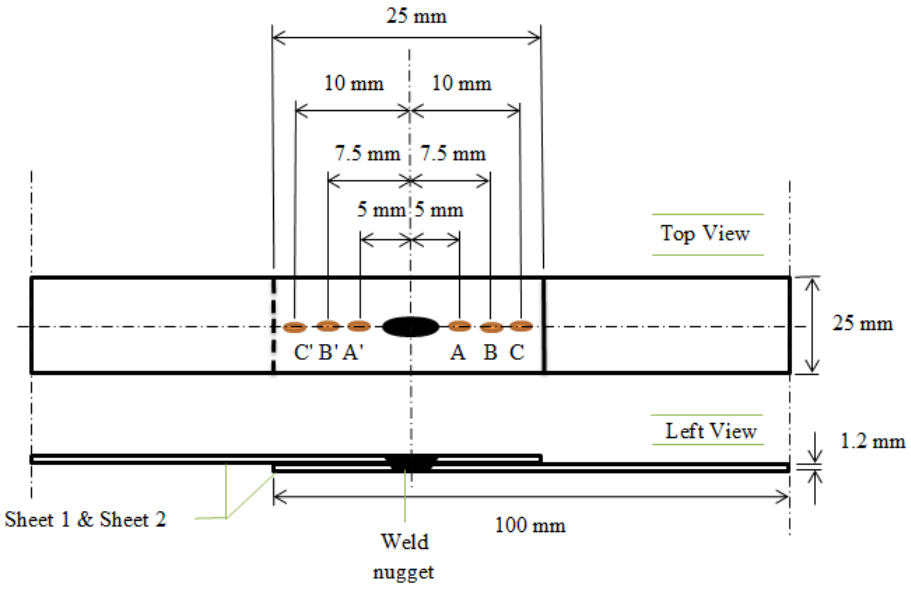

Figure 1: The located points on plate for X-ray diffraction measurements

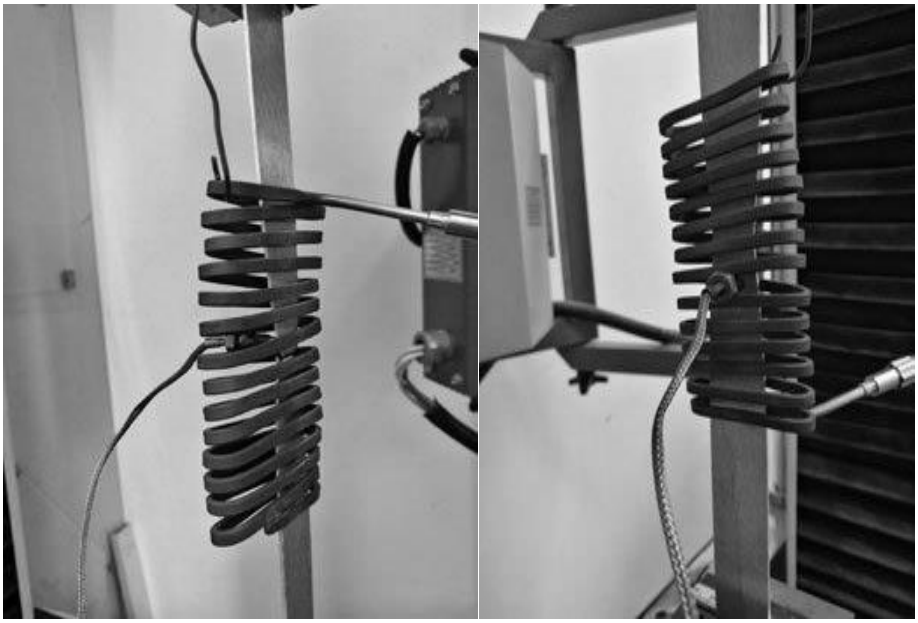

Figure 2: The temperature dependent tensile test

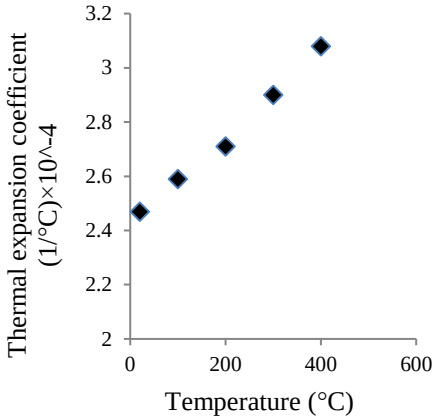
Thermal expansion coefficient (1/°C)×10^-4
3.2
3
2.8
2.6
2.4
2.2
2
0
200
400
600
Temperature (°C)

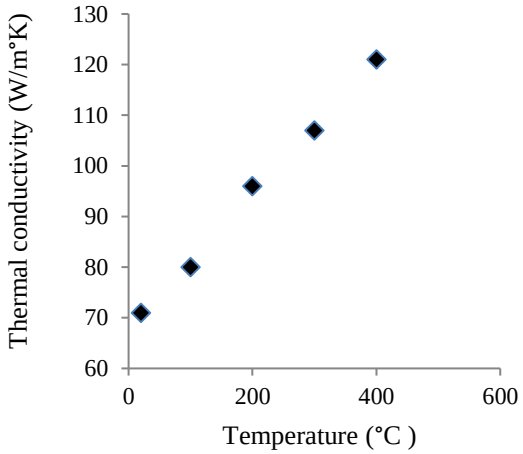
Thermal conductivity (W/m°K)
130
120
110
100
90
80
70
60
0
200
400
600
Temperature (°C)

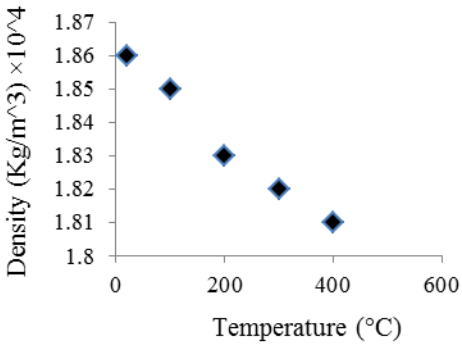
Density (Kg/m^3) ×10^4
1.87
1.86
1.85
1.84
1.83
1.82
1.81
1.8
0
200
400
600
Temperature (°C)

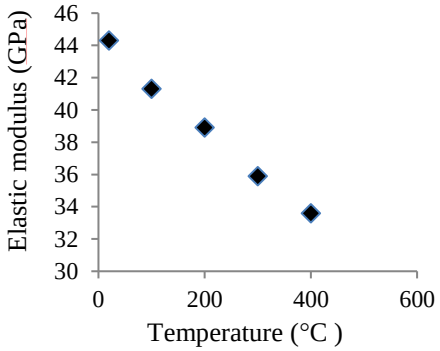
Elastic modulus (GPa)
46
44
42
40
38
36
34
32
30
0
200
400
600
Temperature (°C)

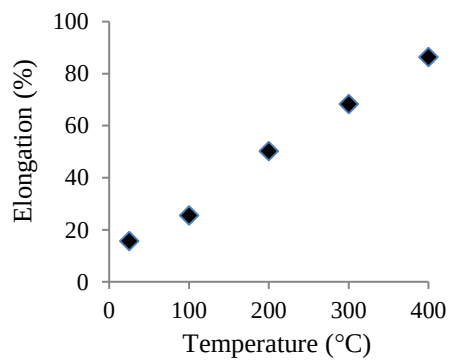
Elongation (%)
100
80
60
40
20
0
0
100
200
300
400
Temperature (°C)

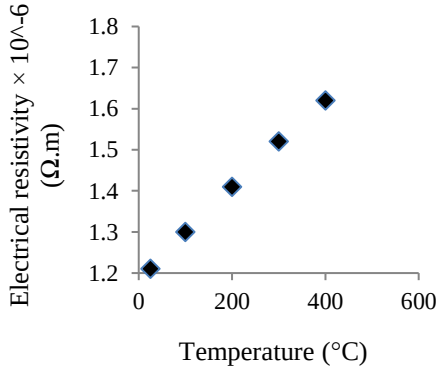
Electrical resistivity × 10^-6 (Ω.m)
1.8
1.7
1.6
1.5
1.4
1.3
1.2
0
200
400
600
Temperature (°C)

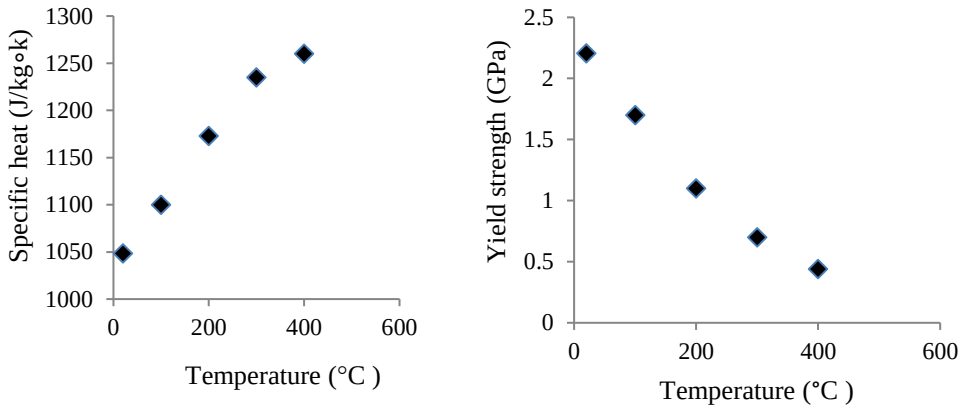

Figure 3: Experimentally determined thermophysical and thermomechanical properties of AZ61 Mg alloy

3 Finite element model

RSW exerts high temperature cycles on the welding structures because of its concentrated and localized heating nature. This process causes nonlinearities in mechanical behavior of the material, which makes it very difficult to be studied analytically. In fact, the analytic study of RSW contains many equations such as electrical, thermal, and structural that must be simplified to be solved, and this would cause significant errors in final results. For this reason, numerical techniques have been developed and adopted. The model geometry adopted in this work is shown in Fig. 4. Due to the symmetric axis, one half of the sample considered for modeling.

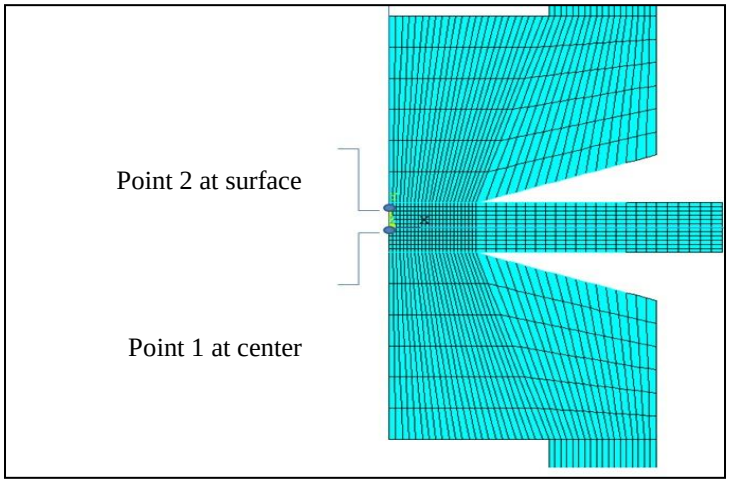

Figure 4: Axisymmetric FE model used in the calculations; points 1 and 2 are two points on the center of weld nugget and surface of sheet metal, respectively

Since the RSW process is a complex phenomenon involving thermal, electrical, and mechanical properties, an incremental fully-coupled mechanical-electrical-thermal FE model has been used in this study. Eq. (1) presents the governing equation for calculation of the thermal analysis:

$$\rho C \frac{\partial T}{\partial t} = \frac{\partial}{\partial r}\left(K \frac{\partial T}{\partial r}\right) + \frac{K}{r}\frac{\partial T}{\partial r} + \frac{\partial}{\partial z}\left(K \frac{\partial T}{\partial z}\right) + \dot{q}(v) \tag{1}$$

Where, ρ is the materials density, C is the heat capacity, T is the temperature, K is the thermal conductivity and $\dot{q}(v)$ is the internal heat generation rate per unit volume. Based on the Fourier isotropic nonlinear relation of temperature density, thermal boundary conditions can be shown by Eq. (2):

$$q = -K\nabla T \tag{2}$$

And the equation for the surface boundary conditions is:

$$q = -K \frac{\partial T}{\partial n} \tag{3}$$

Where, q is the thermal flux on the surface and n is the external normal surfaces vector. The governing equation for the calculation of the electrical potential φ can be presented by Eq. (4):

$$\frac{\partial}{\partial r}\left(C_e \frac{\partial \varphi}{\partial r}\right) + \frac{C_e}{r}\frac{\partial \varphi}{\partial t} + \frac{\partial}{\partial z}\left(C_e \frac{\partial \varphi}{\partial z}\right) = 0 \tag{4}$$

Where, C_e is the electrical conductivity, r is the radial distance and z is the distance in the axis direction. The following matrix for coupling of the thermal and the electrical problems is:

$$\begin{bmatrix} C^t & 0 \\ 0 & 0 \end{bmatrix} \begin{Bmatrix} \dot{T} \\ \dot{V} \end{Bmatrix} + \begin{bmatrix} K^t & 0 \\ 0 & K^v \end{bmatrix} \begin{Bmatrix} T \\ V \end{Bmatrix} = \begin{Bmatrix} \{Q\} \\ \{I\} \end{Bmatrix} \tag{5}$$

Where, $[C^t]$ is the special heat matrix, $[K^t]$ is the thermal conductivity matrix, $[K^v]$ is the electricity matrix, $\{T\}$ is the temperature vector, $\{V\}$ is the electrical potential vector, $\{Q\}$ is the heat flux vector and $\{I\}$ is the electrical current vector. Based on the equilibrium relation of the stress, the mechanical analysis can be shown by Eq. (6):

$$\nabla\sigma(r,t) + b(r,t) = 0 \tag{6}$$

Where σ is the stress, b is the force and r is the coordinate vector. And also the material properties equation based on the thermal-elastic-plastic theory is as follows:

$$d\{\sigma\} = [D]d\{\varepsilon\} - \{C\}dT \tag{7}$$

$$\{C\} = -[D^e]\left(\{\alpha\} + \frac{\partial [D^e]^{-1}}{\partial T}\{\sigma\}\right) \tag{8}$$

Where, $\{\sigma\}$ is the stress vector, $[D]$ is the elastic-plastic matrix, $\{\varepsilon\}$ is the strain vector, $[D^e]$ is the elastic matrix and $\{\alpha\}$ is the thermal expansion coefficient.

In the FE model, the whole steps of RSW process have been considered including squeeze, welding, holding, and cooling. RSW begins with squeezing step, which is performed by mechanical FE model. Results of this step are deformation, contact pressure, and size of contact areas. These data have been considered as initial conditions for further welding cycle. In the welding cycle, a root mean square electrical current according to Eq. (9) has been uniformly applied at the top surface of the upper electrode. The electrical current reaches the bottom surface of the lower electrode where the voltage is zero after passing through the contact area between the electrode-sheet and sheet-sheet.

$$I = I_m \sin(2\pi f t) = \sqrt{2} I_{rms} \sin(2\pi f t) \tag{9}$$

Where f is the frequency and I, I_m and I_{rms} are the real electrical current, the peak of the electrical current and the root mean square electrical current respectively.

The result of the electrothermal FE model is the temperature distribution. The temperature distribution has been used as a preload for thermomechanical FE model. The results of this FE model are deformations and the size of contact regions which have been reserved and utilized for the next increment of electrothermal FE model as an updated preload. The loop continues up to the end of welding time. At the holding cycle, pressure of the electrodes is sustained to form the nugget while the electrical current has been turned off. At the cooling step, the electrodes have been removed from the contact areas by birth and death element technique. In this step, sheets have been cooled down by convection to reach ambient temperature. The temperature gradient then causes residual stresses. At the end of all steps, the residual stress distribution can be extracted from the FE model.

The plane182 and plane67 element types have been utilized for mechanical and electrothermal analysis respectively. The Targe169 and Conta171 element types have been used to display contact areas on the electrode-workpiece interfaces and workpiece-workpiece faying surfaces. Temperature dependent electrical contact conductance (ECC) and thermal contact conductance (TCC) of copper electrode and magnesium AZ61 alloy have been used in contact area [Karimi, Sedighi and Afshari (2015)]. Also, the imposed boundary conditions are presented in Fig. 5.

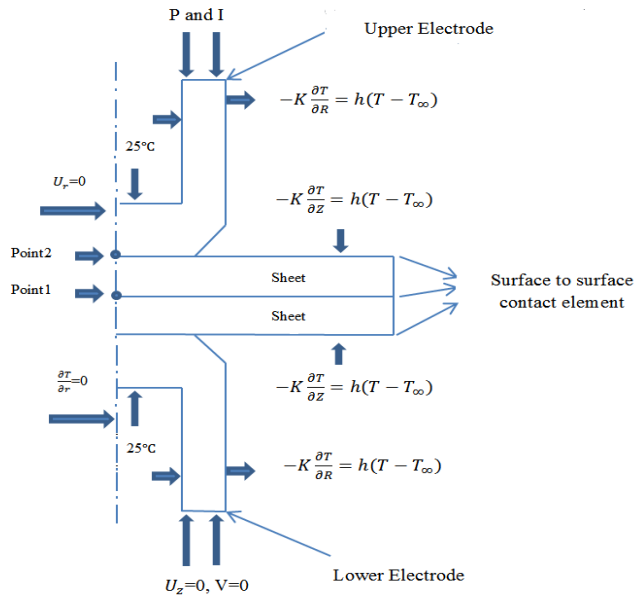

Figure 5: Imposed boundary condition on FE model

In the FE model, shape and size of the elements have important effect on the solution convergence. Mesh sensitivity analysis has been performed with different number of elements (with coarser up to finer elements). Fig. 6 shows that the model with 732 elements is the optimum number of mesh because of no significant temperature change.

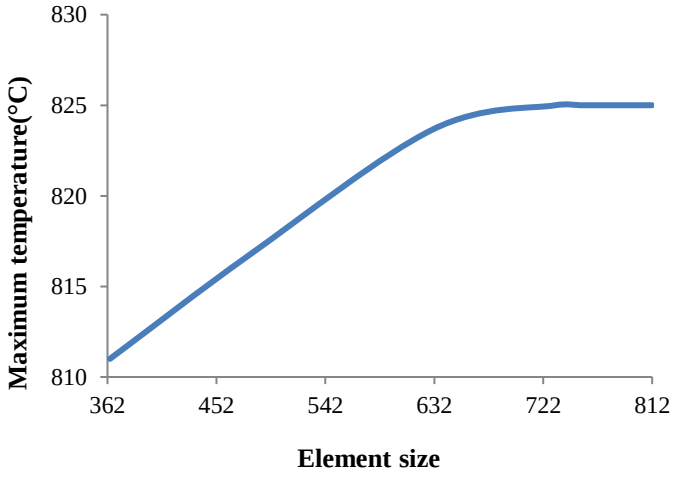

Figure 6: The mesh sensitivity diagram in electrothermal step (welding current: 16 KA; welding time: 16 cycles; electrode force: 1130 N)

4. Results

First, the FE model has been validated by the experimental data obtained from the welding size and residual stresses measuring tests. As Fig. 7 illustrates a good agreement has been detected between the nugget size and shape obtained from the experimental test and FE model. It is important to indicate that the melting point of AZ61 magnesium alloy supposed to be as 650°C and the nugget size has been obtained from the FE model at the end of welding cycle. So the negligible difference between the results occurs because of shrinkage in the experimental test when the nugget cools down to the ambient temperature. In addition, the measured residual stresses from XRD and predicted residual stresses from FE are presented in Tab. 2. The results presented in this table confirm that the FE model has a good reliability to predict the residual stresses in RSW of AZ61 alloy.

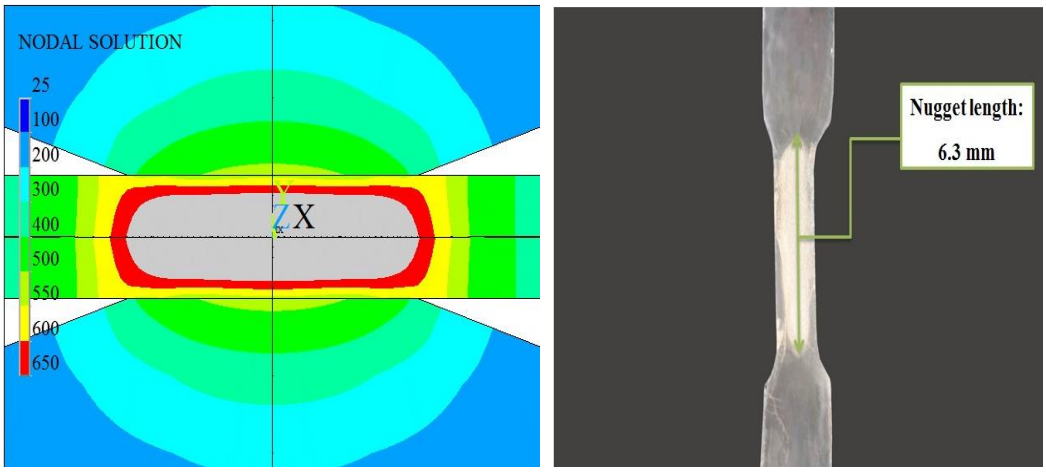

Figure 7: The comparison between FE model and experimental nugget size.

Table 2: Comparison of max principal residual stress obtained from experimental, FE model and the errors

	Experimental test (MPa)			FE model (MPa)			Errors (%)			
Samples	Mean of point A&A'	Mean of point B&B'	Mean of point C&C'	Mean of point A&A'	Mean of point B&B'	Mean of point C&C'	Mean of point A&A'	Mean of point B&B'	Mean of point C&C'	Average of errors
Sample 1	126	41	14	114.14	38.34	13.81	9.4	6.4	1.35	5.72
Sample 2	110	46	15	98.31	41.6	14.22	10.6	9.6	5	8.4

Fig. 8 shows the temperature and the longitudinal residual stress histories for two points: the center of weld nugget and the surface of sheet metal (Fig. 4). In Fig. 8a the maximum temperatures for both points have been reached the end of welding cycle, and they have been decreased down to the end of the holding cycle. Also, these points have equal magnitude and trend at the end of the cooling cycle.

The maximum longitudinal compressive residual stress has been occurred at the welding cycle, and also located at the center of nugget (Fig. 8b). However, the compressive residual stresses reduce, the tensile residual stresses rise up while the time increases.

The temperature reaches to the maximum value at the end of the welding cycle, so the materials in fusion zone tend to expand. The major factors controlling this expansion are temperature and electrode force. The expansion is confronted by relatively cold surrounding materials and these interactions lead to compressive residual stresses. After the welding cycle, there is a decrease in magnitude of compressive residual stresses. At the holding cycle and also cooling cycle, the shrinkage occurs when the nugget cools down and this phenomenon is confronted by relatively cold surrounding materials and these interactions lead to tensile residual stresses as shown in Fig. 8b. At the holding cycle copper electrodes have a significant effect on cooling rate as heat sinks.

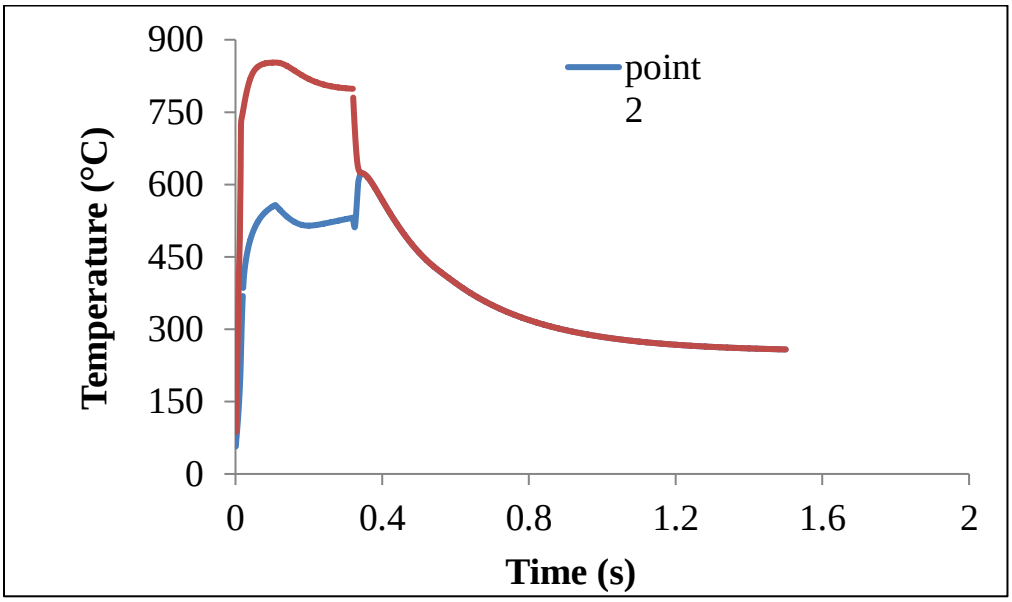

(a)

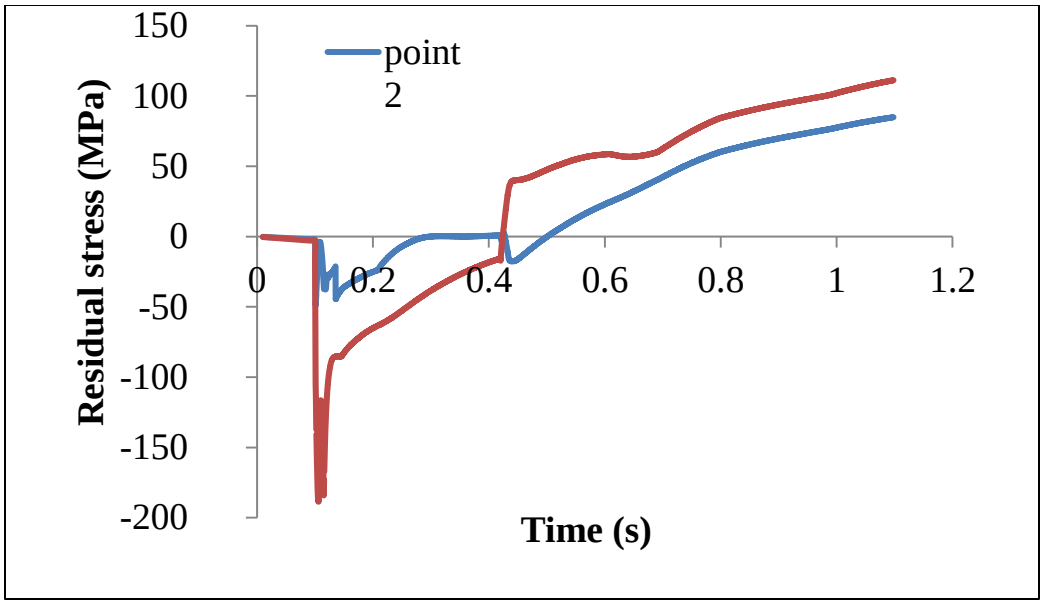

(b)

Figure 8: (a) Temperature histories and (b) Stress histories of point 1 (TEMP center, SX_center) and point 2 (TEMP_surface, SX_surface)

At the holding cycle, a high thermal gradient occurs between the sheet surface contacts and the other sheet regions. These regions, the top and the bottom of the sheet, have direct contact with the electrodes. So, they have been cooled very fast in comparison to the hottest region such as the weld nugget. This thermal gradient remains till the electrodes are removed. In this step, there is no contact between sheet and electrodes. Therefore, the temperature of the sheet surface contacts quickly increases while temperature in the weld area reduces. After holding cycle, the temperature of these points has equal magnitude and same trend. They fall down to the ambient temperature at the cooling cycle as shown in Fig. 8a.

In spite of aluminum alloys, which different changes of residual stresses have been detected at center-line and surface-line [Ranjbar Nodeh, Serajzadeh and Kokabi (2008)]; for magnesium alloys, reduction in both lines have been discovered as shown in Fig. 8. Moreover, Fig. 9 clearly shows that there is a reduction of residual stresses inside and outside of the nugget zone by moving to the end of the sheet.

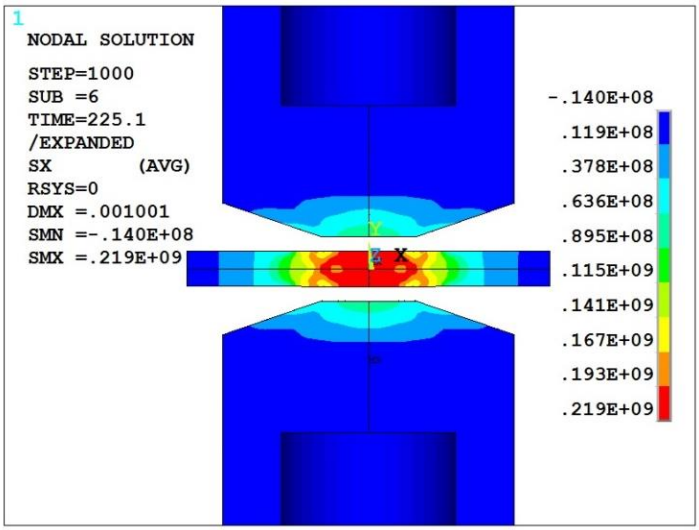

Figure 9: Residual stress distribution for sample 2

However, there are many influential parameters in RSW, in this study the effects of welding current, welding time, and electrode force have been investigated on the maximum tensile residual stress which arises at the center of nugget. Figs. 10, 11 and 12 present the effects of the welding time, welding current, and electrode force on the maximum tensile stress respectively. Fig. 10 shows that the maximum tensile residual stresses are reduced by increasing the welding time. However by improving the welding time during the welding cycle the heat raises according to the Joule's heat law, the produced heat in nugget transfers to the outside region more quickly. This heat transfer leads to a further decrease in the temperature gradient between the nugget and the surrounding regions which reduce the resultant residual stress.

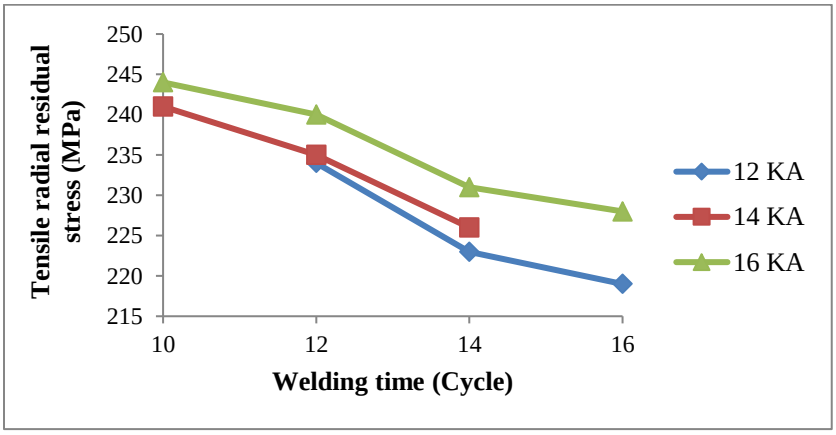

Figure 10: The effect of welding time on the maximum tensile residual stress (electrode force: 848 N)

Fig. 11 displays that the tensile residual stress in welded joints rises by improving the welding current. As the welding current increases, the heat produced in nugget rises, and thereby the gradient of temperature between nugget and its surroundings areas increases. Fig. 12 illustrates that the maximum tensile residual stress declines by increasing the applied electrode force. Actually, increasing the electrode force subsequently raises the compressive stresses at the welded area.

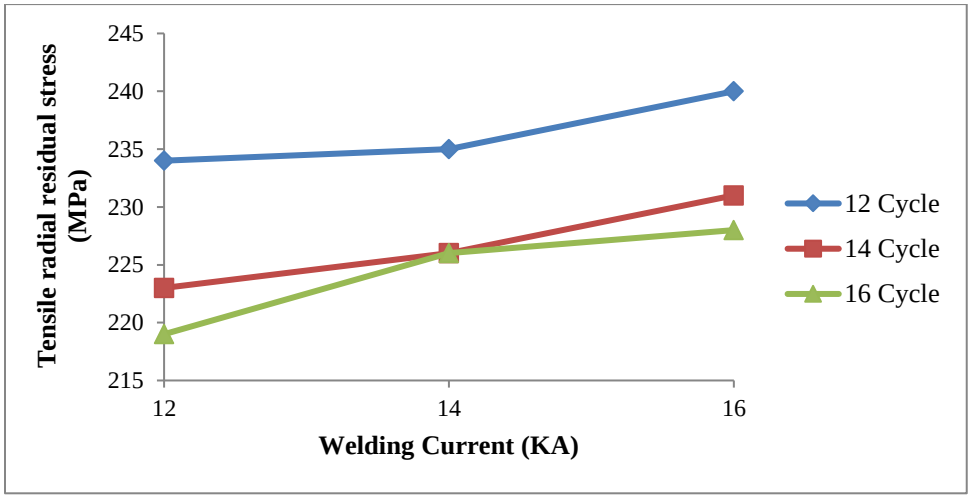

Figure 11: The effect of welding current on the maximum tensile residual stress (electrode force: 848 N)

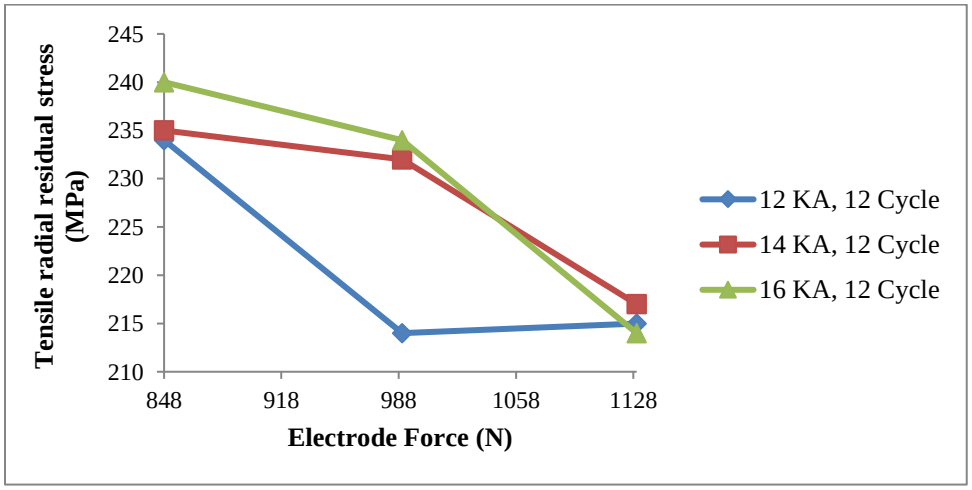

Figure 12: The effect of electrode force on the maximum tensile residual stress

5 Conclusion

In this study a structural-thermal-electrical FE model has been utilized to study the distribution of residual stresses in resistance spot welded AZ61 magnesium alloy sheet.

Also, the experimental measurements have been carried out by using XRD to validate the FE model. Moreover, the model has been utilized to investigate the effects of welding parameters such as welding current, welding time, and electrode force on the maximum tensile radial residual stress. The obtained results show that:

(1) The presented FE model is reliable to predict the nugget size and distribution of residual stresses occurred during the RSW process. There is a good agreement between the results obtained from the FE model and the experimental tests.

(2) While the maximum tensile residual stresses occurred in the nugget center, the reduction inside and outside of nugget zone are detected by moving to the end of the sheet.

(3) In order to decrease the tensile radial residual stresses in the welding area, an upper limit of welding time and electrode force are required while the welding current should be in its minimum level.

References

Afshari, D.; Sedighi, M.; Karimi, M. R.; Barsoum, Z. (2013): On residual stresses in resistance spot-welded aluminum alloy 6061-T6: experimental and numerical analysis. *Journal of Materials Engineering Performance*, vol. 22, no. 12, pp. 3612-3619.

Asle Zaeem, M.; Nami, M. R.; Kadivan, M. H. (2007): Prediction of welding buckling distortion in thin wall aluminum T joint. *Computational Material Science*, vol. 38, no. 4, pp. 588-594.

ASME (2002): *Qualification Standard for Welding and Brazing Procedures, Welders, Brazers and Welding and Brazing Operators*. ASME IX, American Society of Mechanical Engineers.

Barsoum, Z. (2013): Residual stress prediction and relaxation in welded tubular joint. *Welding World*, vol. 51, pp. 23-30.

Cha, B. W.; Na, S. J. (2003): A study on the relationship between welding conditions and residual stress of resistance spot welded 304-type stainless steels. *Journal of Manufacturing Systems*, vol. 22, no. 3, pp. 181-189.

Florea, R. S.; Hubbard, C. R.; Solanki, K. N.; Bammann, D. J.; Whittington, W. R. et al. (2012): Quantifying residual stresses in resistance spot welding of 6061-T6 aluminum alloy sheets via neutron diffraction measurements. *Journal of Materials Processing Technology*, vol. 212, no. 11, pp. 2358-2370.

James, M. N.; Webster, P. J.; Hughes, D. J.; Chen, Z.; Ratel, N. et al. (2006): Correlating weld process conditions, residual strain and stress, micro structure and mechanical properties for high strength steel-the role of diffraction strain scanning. *Material Science Engineering*, vol. 427, no. 1-2, pp. 16-26.

Karimi, M. R.; Sedighi, M.; Afshari, D. (2015): Thermal contact conductance effect in modeling of resistance spot welding process of aluminum alloy 6061-T6. *International Journal of Advanced Manufacturing Technology*, vol. 77, pp. 885-895.

Kramar, T.; Vondrous, P.; Kolarikava, M. (2015): Resistance spot welding of

magnesium alloy AZ61. *Modern Machinery Science*, no. 1, pp. 596-599.

Manladan, S. M.; Yusof, E.; Ramesh, S.; Fadzil, M. (2016): A review on resistance spot welding of magnesium alloys. *International Journal of Advanced Manufacturing Technology*, vol. 86, no. 5-8, pp. 1805-1825.

Moharrami, R.; Hemmati, B. (2017): Numerical stress analysis in resistance spot-welded nugget due to post-weld shear loading. *Journal of Manufacturing Processing*, vol. 27, pp. 284-290.

Moshayedi, H.; Sattari-far, I. (2014): Resistance spot welding and the effects of welding time and current on residual stresses. *Journal of Materials Processing Technology*, vol. 214, no. 11, pp. 2542-2552.

Pakkanen, J.; Vallant, R.; Kiein, M. (2016): Experimental investigation and numerical simulation of resistance spot welding for residual stress evaluation of DP1000 steel. *Welding World*, vol. 60, no. 3, pp. 393-402.

Parmar, R. S. (1999): *Welding Processes and Technology*. 2nd ed., Khanna Publishers, India.

Ranjbar Nodeh, I.; Serajzadeh, S.; Kokabi, A. H. (2008): Simulation of welding residual stresses in resistance spot welding, FE modeling and x-ray verification. *Journal of Materials Processing Technology*, vol. 205, no. 1-3, pp. 60-69.

Satonaka, S.; Lwamoto, C.; Matsumoto, Y.; Murakami, G. I. (2012): Resistance spot welding of magnesium alloy sheets with cover plates. *Welding World*, vol. 56, no. 7-8, pp. 44-50.